

# Magnon dispersion and spin transport in $\text{CrCl}_3$ bilayers under different strain-induced magnetic states

Verena Brehm,<sup>1,\*</sup> Stefan Stagraczyński,<sup>2</sup> Józef Barnaś,<sup>2</sup> Anna Dyrdał,<sup>2</sup> and Alireza Qaiumzadeh<sup>1</sup>

<sup>1</sup>*Center for Quantum Spintronics, Department of Physics,  
Norwegian University of Science and Technology, Trondheim, Norway*

<sup>2</sup>*Faculty of Physics, ISQI, Adam Mickiewicz University in Poznań,  
ul. Uniwersytetu Poznańskiego 2, 61-614 Poznań, Poland*

Atomically-thin van der Waals magnetic materials offer exceptional opportunities to mechanically and electrically manipulate magnetic states and spin textures. The possibility of efficient spin transport in these materials makes them promising for the development of novel nanospintronics technology. Using atomistic spin dynamics simulations, we investigate magnetic ground state, magnon dispersion, critical temperature, and magnon spin transport in  $\text{CrCl}_3$  bilayers in the absence and presence of compressive and tensile strains. We show that in the presence of mechanical strain, the magnon band gap at the  $\Gamma$  point and the critical temperature of the bilayer are increased. Furthermore, our simulations show that the magnon diffusion length is reduced in the presence of strain. Moreover, by exciting magnons through the spin Seebeck effect and spin Hall-induced torque, we illustrate distinctions between magnon spin transport in the antiferromagnetic state, under compressive strains, and ferromagnetic states, under tensile strains or in the unstrained case.

## I. INTRODUCTION

Two-dimensional (2D) magnetic systems [1–4] represent a novel and promising platform for the next generation of magnonic [5–7] and spintronic [8–10] nanodevices. This is attributed to their highly tunable magnetic and electronic properties, making them an ideal testbed for probing novel exotic phenomena [11–17]. With the demonstration of long-range magnetic order in monolayer and few-layer thickness van der Waals (vdW) materials [4, 11, 18–20], the class of chromium trihalides ( $\text{CrX}_3$ ,  $\text{X}=\text{Cl}, \text{Br}, \text{I}$ ) with honeycomb lattice structure has come into focus. It has been shown that in contrast to  $\text{CrI}_3$  that shows a topological band gap in the magnon dispersion at the Dirac points [21–24],  $\text{CrCl}_3$  hosts massless Dirac magnons at the K and K' points [25, 26].

In particular, the possibility of tuning the magnonic properties in these layered magnetic vdW materials through external stimuli, such as electrostatic gating, magnetic fields, and mechanical strains [16, 27–38], is intriguing for application in novel nanospintronic technology. Recent theoretical studies have demonstrated controllable manipulation of the magnetic ground state in the  $\text{CrCl}_3$  mono- and bilayer through mechanical strains [16, 38]. Biaxial strains have the potential to induce transitions between ferromagnetic (FM) and antiferromagnetic (AFM) phases. Additionally, they can alter the magnetic ground state from uniaxial out-of-plane (OOP) to biaxial easy-plane (EP) magnetic states.

Although there are several theoretical and experimental studies on the static magnetic behavior of these materials, only a few recent experiments have explored magnon spin transport in atomically-thin vdW FM and AFM materials via either thermal [39–42] or electrical

[43] mechanisms. To demonstrate the potential of vdW magnets for spintronic and magnonic nanotechnology, additional theoretical and experimental studies under various external stimuli are essential.

In order to make a theoretical ground for further studies in magnon dynamics in vdW materials, in this paper, we investigate magnon transport in a bilayer of  $\text{CrCl}_3$  under biaxial compressive and tensile strains. Using atomistic spin dynamics simulations [44], we compute magnon dispersion and magnon transport, where the latter is excited through the thermal spin Seebeck effect (SSE) [45–55] and the electrical (anomalous) spin-Hall torque (SHT) mechanism [56–61]. Three sets of effective spin parameters represent three magnetic states that can be achieved through mechanical strains [38]: an EP AFM state in the presence of a compressive strain (negative strain), an EP FM state at the absence of strain, and an OOP FM state in the presence of a tensile strain (positive strain). It is worthwhile to mention that while we use  $\text{CrCl}_3$  spin interaction parameters in this study, the qualitative findings of this article can be applied to a wide class of vdW magnetic layers.

The rest of the paper is structured as follows: First, we present our system setup, its effective spin model, and our spin dynamic simulation method in Section II. In Section III, we compute the magnon dispersion and critical temperature in the  $\text{CrCl}_3$  bilayer under various mechanical strains. In Section IV, we investigate magnon spin transport and compute the magnon diffusion length in different magnetic states of the system. Finally, we discuss and conclude the findings and their practical implications in Section V.

## II. MODEL AND METHOD

This section presents our system geometry, effective spin Hamiltonian, and the atomistic spin dynamic simu-

\* verena.j.brehm@ntnu.no

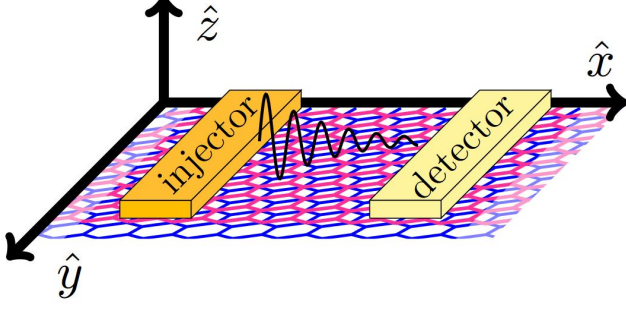


FIG. 1. Schematic setup for magnon spin transport simulation in a  $\text{CrCl}_3$  bilayer with honeycomb lattice structure: magnons, denoted by a solid black damped wave, are injected by the left lead through the SSE and/or SHT mechanisms, and propagate via a diffusive transport to the right lead along the  $x$  direction, where they are detected through the inverse (anomalous) spin Hall effect.

lation method employed to calculate magnon dispersion and magnon spin transport.

#### A. Device geometry and setup

To investigate spin transport in a  $\text{CrCl}_3$  bilayer, we use a setup depicted in Fig. 1. It emulates experimental systems where spin-transport measurements are performed in the so-called nonlocal geometry [43, 57, 60]. In this geometry, magnons are injected from the left lead via either SSE [45, 46, 56] and/or the (anomalous) SHT [56, 61, 62] and propagate through the system along the  $x$  direction until the magnon spin current signal is detected on the detector lead. In magnon spin transport experiments, the injector and detector can be either a heavy metal or an FM metal with strong spin-orbit coupling. In the first case, the (inverse) spin Hall effect only allows for the injection (detection) of in-plane spin signals [62]. However, in the second case, the (inverse) anomalous spin Hall effect enables the injection (detection) of OOP spin signals [61]. We will address spin injection and detection processes in more detail in the next sections.

#### B. Effective spin Hamiltonian of $\text{CrCl}_3$ bilayer

A  $\text{CrCl}_3$  bilayer consists of two atomic planes of magnetic Cr atoms surrounded by nonmagnetic Cl atoms. Within each atomic plane, the magnetic Cr atoms are arranged on a honeycomb lattice, and the two planes are stacked rhombohedrally. The system thus has four spins per magnetic unit cell. The effective spin interaction between magnetic Cr atoms can be modeled by the

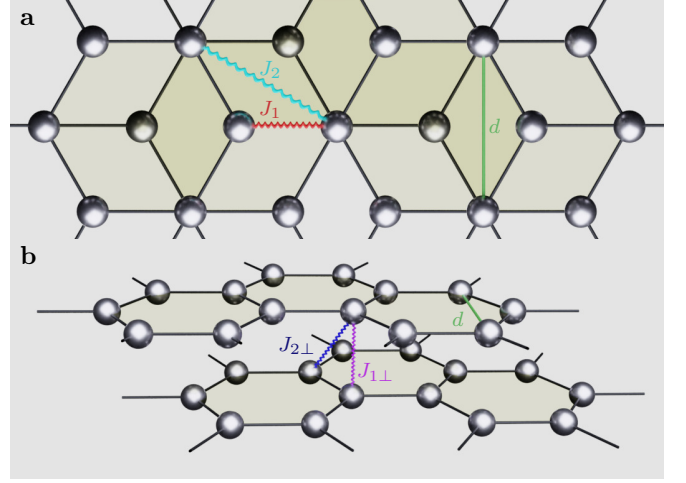


FIG. 2. Atomic model depicting magnetic Cr atoms arranged in a honeycomb lattice within a  $\text{CrCl}_3$  bilayer with rhombohedral stacking. Figures present a top view (a) and a perspective view (b). The red and cyan wavy lines in (a) illustrate the *intralayer* NN,  $J_1$ , and NNN,  $J_2$ , respectively. The purple and blue wavy lines in (b) denote *interlayer* NN,  $J_{1\perp}$ , and NNN,  $J_{2\perp}$ , coupling, respectively.  $d \approx 0.6$  nm is the lattice constant.

following Hamiltonian [38, 63]:

$$\begin{aligned} \mathcal{H} = & - \sum_{i < j} J_{ij} \mathbf{S}_i \cdot \mathbf{S}_j - K_x \sum_i (\mathbf{S}_i \cdot \hat{e}_x)^2 \\ & - K_z \sum_i (\mathbf{S}_i \cdot \hat{e}_z)^2. \end{aligned} \quad (1)$$

In this spin Hamiltonian,  $\mathbf{S}_i$  is a unit vector that carries the direction of the atomic magnetic moment at site  $i$ ,  $J_{ij}$  denotes the symmetric Heisenberg exchange coupling between sites  $i$  and  $j$ . This exchange term includes the *intralayer* nearest-neighbor (NN)  $J_1$  and next-nearest neighbor (NNN)  $J_2$  coupling, as well as *interlayer* NN  $J_{1\perp}$ , and NNN  $J_{2\perp}$  coupling, see Fig. 2. We also introduce two single-ion magnetic anisotropy axes along the in-plane  $x$  and OOP  $z$  directions, parameterized by  $K_x$  and  $K_z$ , respectively. Since the Dzyaloshinskii–Moriya interactions are very weak in this system, we neglect them in our effective spin Hamiltonian [38, 64, 65].

Mechanical strains can modify both the sign and strength of Heisenberg exchange coupling  $J_{ij}$  and magnetic anisotropy  $K_{x(z)}$  [38]. The exchange coupling parameters  $J_{ij}$  are modified by strain, leading to an AFM order at -5% strain, and an FM order at 0% and +5% strain [38]. Furthermore, for both the unstrained and the -5% compressive strained case, the magnetic ground state lies along the  $x$  direction inside the easy  $x$ - $y$  plane, with  $K_x > 0$  and  $K_z < 0$ , which leads to an EP magnetic state. For the +5% tensile strain case, the magnetic ground state lies along the  $z$  direction,  $K_z > 0$ , resulting in an OOP FM state. The parameters used in our spin dynamics simulations are listed in Table I. In order to reduce computational cost, we do not include dipolar

TABLE I. The value of spin interaction parameters under various strains [38], introduced in the spin Hamiltonian Eq. (1): NN and NNN intra-layer,  $J$ , and inter-layer,  $J_{\perp}$ , Heisenberg exchange parameters, and magnetic anisotropy  $K_{x(z)}$ . The magnetic ground state is sketched using the sublattice spins.

Parameter	0% strain	+5% strain	-5% strain
$J_1$	1.53 meV	2.39 meV	-2.94 meV
$J_2$	0.29 meV	0.24 meV	0.44 meV
$J_{1\perp}$	0.07 meV	0.11 meV	0.01 meV
$J_{2\perp}$	0.07 meV	0.08 meV	0.07 meV
$K_x$	0.06 meV	0	0.06 meV
$K_z$	-0.5 meV	1.25 meV	-4.75 meV
Magnetic state	$\Rightarrow$	$\Uparrow\Uparrow$	$\Leftarrow$
	EP FM	OOP FM	EP AFM

interactions in our simulations. This can be justified by the fact that in 2D bulk vdW magnetic materials, dipolar interactions are mainly reduced to an effective magnetic anisotropy that slightly shifts the magnon spectrum [66, 67]. This has no qualitative impact on our findings, since it only leads to a minor modification of the magnetic anisotropy constants.

### C. Atomistic spin dynamics simulations

Spin dynamics at finite temperature is governed by the stochastic Landau–Lifshitz–Gilbert (sLLG) equation [44]:

$$\frac{\partial \mathbf{S}_i}{\partial t} = -\frac{\gamma}{1 + \alpha_0^2} [\mathbf{S}_i \times \mathbf{B}_i^{\text{eff}} + \alpha_0 \mathbf{S}_i \times (\mathbf{S}_i \times \mathbf{B}_i^{\text{eff}})], \quad (2)$$

where  $\gamma$  is the gyromagnetic ratio,  $\alpha_0$  denotes the Gilbert damping parameter, and  $\mathbf{B}_i^{\text{eff}}$  is the effective magnetic field at site  $i$ . The effective field  $\mathbf{B}_i^{\text{eff}}$  consists of two terms: a deterministic term, related to the spin Hamiltonian, and a stochastic term, related to the thermal fluctuations,

$$\mathbf{B}_i^{\text{eff}} = -\frac{1}{\mu_s} \frac{\partial \mathcal{H}}{\partial \mathbf{S}_i} + \boldsymbol{\xi}_i^{(\text{th})}, \quad (3)$$

where  $\mu_s$  is the atomic spin moment. The stochastic term at the low-frequency regime is modeled as Gaussian thermal noise,

$$\langle \boldsymbol{\xi}_i^{(\text{th})}(t) \rangle = 0, \quad (4a)$$

$$\langle \xi_{i,m}^{(\text{th})}(t) \xi_{j,n}^{(\text{th})}(t') \rangle = \frac{2\alpha_0 k_B T}{\gamma \mu_s} \delta_{ij} \delta_{mn} \delta(t - t'), \quad (4b)$$

where  $k_B$  is the Boltzmann constant and  $m, n = \{x, y, z\}$  denote spatial components.

To investigate the spin dynamics within our system, we utilize a stochastic Heun algorithm implemented in the VAMPIRE code [44, 68] for the numerical solution of the sLLG equation.

### D. Spin injection and spin detection

(i) *Detection of spin signal via spin pumping* – The spin signal at the distance  $x$  from the injector is determined by computing the local spin accumulation at the detector interface [69–71],

$$\boldsymbol{\mu}(x) := G_r^{\uparrow\downarrow} \sum_{i=1}^N \left\langle [\mathbf{S}_i(t) \times \dot{\mathbf{S}}_i(t)] \right\rangle_t, \quad (5)$$

where the sum runs over sites at the interface between the detector and the magnetic bilayer,  $G_r^{\uparrow\downarrow}$  is the real part of the spin mixing conductance [72], and  $\langle \cdot \rangle_t$  denotes a time average that is conducted after steady state is reached. As we already mentioned, the spin accumulation at the interface is converted to a charge voltage at the lead via the inverse (anomalous) Hall effect. In this article, we are interested in the dc spin signal, and thus, we only present the component of the spin accumulation that is parallel to the magnetic ground state.

(ii) *Injection of spins via SSE and SHTs* – The spin signal can be generated through a thermal gradient, via SSE, and/or electrically through spin Hall effects, via (anomalous) SHTs.

In the first scenario, a temperature gradient is applied to generate a spin voltage through the so-called SSE [45, 46, 48–51, 56, 73]. The increase in temperature in the injector results in a higher local occupancy of thermal magnon modes compared to the rest of the system, which maintains a lower temperature. This results in an incoherent magnon current flowing from the hotter side toward the cooler side [52–55].

In the second scenario, the charge-induced (anomalous) spin Hall effect in the injector layer gives rise to interfacial spin torques [6, 56, 57]. These SHTs can be modeled using the following effective field [74] that is added to the effective magnetic field, Eq. (3),

$$\mathbf{B}_i^{\tau} = \tau_0^P (\mathbf{p} - \alpha_0 \mathbf{S}_i \times \mathbf{p}) + \tau_0^R (\mathbf{S}_i \times \mathbf{p} + \alpha_0 \mathbf{p}). \quad (6)$$

Here  $\mathbf{p}$  is the spin polarization direction, induced by the (anomalous) spin Hall effect. The first term is the precession-like field, parameterized by  $\tau_0^P$ , and the second term is the relaxation-like field, parameterized by  $\tau_0^R$ . These two parameters are related to the material parameters and charge current density.

The relaxation-like torque is responsible for generating an effective magnon chemical potential [75] at the interface. Consequently, it facilitates the flow of the magnon current through the system. On the other hand, the precession-like torque only adjusts the eigenfrequencies of the magnon eigenstates [74].

In our simulations, we set  $\mathbf{p}$  parallel to the ground-state spin direction. As we discussed earlier, in experiments, an in-plane and OOP spin polarization direction  $\mathbf{p}$  can be generated by spin Hall and anomalous spin Hall effects, respectively [61]. Note that in this scenario, where  $\mathbf{p}$  is parallel to the magnetic ground state, finite thermal

fluctuations are required to generate a finite spin torque at the interface [60].

### III. MAGNON DISPERSION AND CRITICAL TEMPERATURE

To calculate the magnon dispersion through atomistic spin dynamics simulations [44], we set up a  $\text{CrCl}_3$  bilayer system with rhombohedral stacking. First, we determine the magnetic ground state of the system. Following this, we introduce a small random deviation around the equilibrium spin directions. Next, we let spins evolve according to the sLLG equation, Eq. (2), and compute the temporal and spatially resolved transverse spin components. Finally, we find the dispersion curve by performing a Fourier transform in both the time and space domains.

The magnon dispersion of the  $\text{CrCl}_3$  bilayer is shown in Fig. 3 for all the three magnetic states. Since the honeycomb magnetic unit cell carries two magnetic atoms, there are two magnon branches per layer, one at low frequencies, acoustic-like, and one at high frequencies, optic-like. Thus, in total, the bilayer system has four magnon branches. Magnon branches can be partially (non)degenerate in some regions of the magnetic Brillouin zone. The degeneracy of the two acoustic-like magnon branches at the  $\Gamma$  point can be lifted by either the interlayer exchange couplings or the presence of a hard-axis magnetic anisotropy. While the easy-axis magnetic anisotropy opens a magnon band gap at the  $\Gamma$  point, the amplitude of the exchange couplings modifies the slope of the branches and also determines the magnon bandwidth.

Figure 3(a) shows the magnon dispersion of the unstrained case, with a biaxial EP FM state. The degeneracy of acoustic-like magnon bands around the  $\Gamma$  point is lifted because of a finite hard-axis magnetic anisotropy  $K_z < 0$  and its lowest branch is gapped because of a finite easy-axis magnetic anisotropy  $K_x > 0$ . Around the K point, there is a massless Dirac-like magnon dispersion with a fourfold degenerate crossing at the K point.

Figure 3(b) presents the magnon dispersion of the bilayer system in the presence of tensile strain with OOP FM state. In this case there is only a uniaxial easy-axis anisotropy  $K_z > 0$  which is larger than its counterpart in the unstrained case and thus creates a larger magnon band gap at the  $\Gamma$  point. The degeneracy of acoustic-like magnon branches around the  $\Gamma$  point is lifted because of interband exchange interactions. The magnon dispersion at the K-point maintains its fourfold degenerate crossing in this case as well. The magnon bandwidth is increased in this case compared to the zero strain case.

Figure 3(c) shows the magnon dispersion of the bilayer system in the presence of compressive strain with a biaxial EP AFM ground state. The linear magnon dispersion around the  $\Gamma$  point, characteristic of AFM magnons, is different from the FM cases with a parabolic dispersion. The magnon gap at the  $\Gamma$  point and lifting the degeneracy

of the two acoustic-like branches are caused by the presence of an easy-axis  $K_x > 0$  and a hard-axis  $K_z < 0$  magnetic anisotropy, respectively.

The characteristics of magnon modes vary across the three distinct magnetic states engineered by mechanical strains. In FM systems, magnon eigenstates have right-handed helicity, whereas in AFM systems, both left- and right-handed helicities are allowed [60, 76]. Moreover, the ellipticity of magnon eigenmodes varies across the three scenarios owing to distinct magnetic anisotropies. In the magnetic easy-axis case, the magnon eigenmodes are circularly polarized. In the easy-plane case, however, magnons are elliptically polarized, attributed to the magnetic hard-axis anisotropy [60, 76].

In our 2D magnetic model, Eq. (1), without long-range dipolar interactions, the magnon gap at the  $\Gamma$  point mainly determines the critical temperature of the magnetic states [77–83], which is dictated by the Hohenberg–Mermin–Wagner theorem [84–86]. Due to variations in Heisenberg exchange couplings and magnetic anisotropies, induced by strain fields, the  $\text{CrCl}_3$  bilayer shows different critical temperatures across its three magnetic states. We find the critical temperature, using specific heat calculations, for three magnetic states, see the Appendix for technical details,

$$T_c^{0\%} \approx 18 \text{ K}, \quad (7a)$$

$$T_c^{+5\%} \approx 26 \text{ K}, \quad (7b)$$

$$T_c^{-5\%} \approx 32 \text{ K}. \quad (7c)$$

These results show the viability of 2D magnetic bilayers for novel magnonic technology. In the next section, we show how the spin angular momentum, as an information carrier, can be transferred by these magnons in the system.

### IV. MAGNON SPIN TRANSPORT IN BILAYER $\text{CrCl}_3$

As we have discussed in Section IID, the spin voltage can be created by either SSE or SHT in a nonlocal geometry setup; see Fig. 1. It is worth mentioning that in SHT experiments, an SSE is also generated because of the parasitic Joule heating created by an applied low-frequency charge current in the injector and contributes to the measured total spin voltage in the detector [6, 56, 57]. To discriminate between the spin voltage induced by nonthermal SHT and thermal SSE, the first- and second-harmonic voltages are measured in the detector, respectively. The even component of the spin voltage, which is quadratic in the applied charge current and related to the thermal SSE contribution, is the average of measured spin signals for two opposite charge current polarities in the injector. The odd component, which is linear in the applied charge current and describes the nonthermal SHT contribution, is computed from the

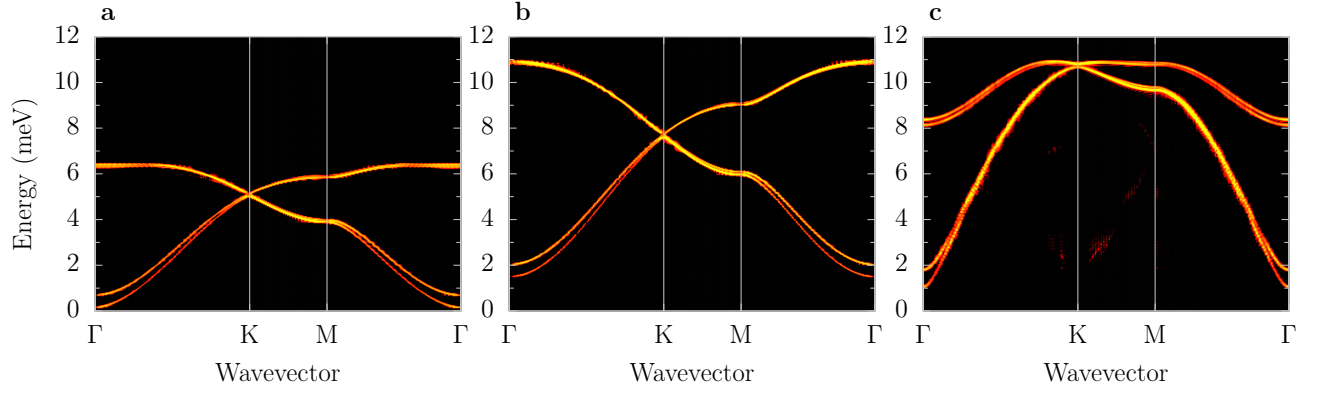


FIG. 3. Magnon dispersion relation for (a) an unstrained case 0% (biaxial EP FM state), (b) a tensile strain +5% (uniaxial OOP FM state), and (c) a compressive strain -5% (biaxial EP AFM state).

TABLE II. Material parameters used for the magnon spin transport simulations.

Quantity	Symbol	Value	Unit
Length	$L_x$	500	nm
Width	$L_y$	50	nm
Lattice constant	$d$	0.6	nm
Time step	$\Delta t$	1	fs
Bulk Gilbert damping [87]	$\alpha_0$	$2 \times 10^{-3}$	-
Gilbert damping at left (right) edge	$\alpha_L(\alpha_R)$	0.5 (0.9)	-
<b>SHT Mechanism</b>			
Spin torques in FM (AFM) state	$\tau_0^P = \tau_0^R$	0.01(0.2)	T
Background temperature	$T_0$	1	K
<b>SSE Mechanism</b>			
Injector temperature	$T_{\text{inj}}$	5	K
Background temperature	$T_0$	1	K

difference between spin voltages generated by two opposite charge current polarities. In the following we also compute these even and odd spin signals.

In the presence of Gilbert damping, magnons diffusely propagate through the system along the  $x$  direction in our setup, Fig. 1. The spatial dependence of nonequilibrium spin accumulation, far from the injector, can be modeled by [88],

$$\delta\bar{\mu}(x) := \frac{\mu(x) - c}{\mu_0} = \exp\left(-\frac{x - x_0}{\lambda}\right), \quad (8)$$

where  $\lambda$  is the magnon spin diffusion length,  $x_0 \gg d$ , and  $c$  is the background thermal equilibrium spin accumulation. The spin accumulation is normalized to  $\mu_0 \equiv \mu(x_0)$ . As we mentioned earlier, we only compute the component of spin accumulation that is parallel to the magnetic ground state in each case.

We utilize the material parameters listed in Table II to simulate magnon transport in our system with a non-local geometry as illustrated in Fig. 1. Figures 4 and 5 depict the outcomes of atomistic spin dynamics simulations illustrating the spin signal, Eq. (5), at the detector

for SSE and SHT mechanisms, respectively, in three magnetic states of the  $\text{CrCl}_3$  bilayer.

(i) *SSE mechanism*: To introduce a temperature gradient across the system, we set the temperature of the injector at  $T_{\text{inj}} = 5$  K. In the biaxial EP and uniaxial OOP FM states, which are magnetic ground states under 0% and +5% strains, respectively, thermally excited incoherent magnons carry a net spin angular momentum that diffuses through the system and creates a spin signal at the detector. Figure 4 shows the spatial dependence of the spin accumulation for two FM states. In the EP AFM state of the  $\text{CrCl}_3$  bilayer, which is the magnetic ground state under a compressive strain of -5%, two AFM magnon eigenstates in Fig. 3(c) are roughly linearly polarized and thus in principle do not carry any spin angular momentum.

It is worth mentioning that even in uniaxial easy-axis AFM systems with two degenerate circularly polarized magnon eigenmodes, the SSE mechanism is unable to generate a finite spin signal. This is due to the equal thermal population of the two degenerate magnon branches [47, 89].

As mentioned earlier, the thermal spin signal in SSE experiments is an even component of the spin voltage,  $\delta\bar{\mu} = (\delta\bar{\mu}(x, +\mathbf{p}) + \delta\bar{\mu}(x, -\mathbf{p}))/2$ . Therefore, for a FM state, the background thermal spin signal,  $c$ , is finite in the spin signal generated by the SSE mechanism, as shown by the dashed lines in the inset of Fig. 4. We extract the magnon diffusion length for the SSE mechanism by fitting the spin accumulation with Eq. (8), see Table III.

(ii) *SHT mechanism*: In the nonthermal SHT mechanism, most of the generated magnons have a well-defined wave vector and frequency determined by the amplitude of the spin torque and the geometry of the injector [60]. Hence, the magnons in the SHT mechanism are not as incoherent as in the thermal SSE mechanism. In the SHT mechanism, the spin polarization  $\mathbf{p}$  must be parallel to the magnetic ground state at a finite temperature background, see Section IID. We set a background temperature  $T_0 = 1$  K in our simulations

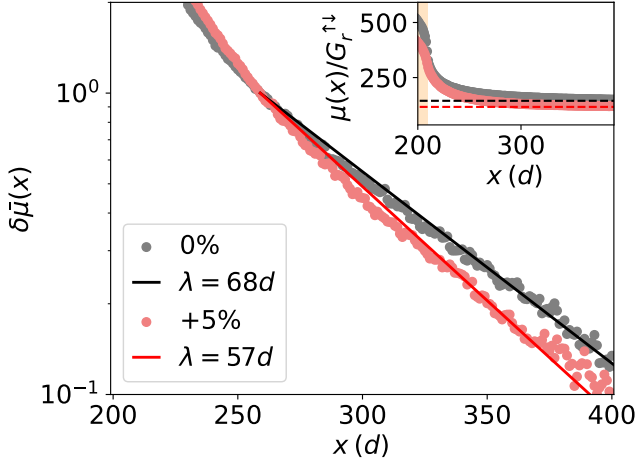


FIG. 4. Spatial dependence of the thermal SSE-induced nonequilibrium spin accumulation for EP (unstrained) and OOP (+5% strain) FM states. There is no spin signal in -5% strain case with an AFM state in this scenario. The extracted spin diffusion length  $\lambda$ , found with Eq. (8), of each case is represented in the legend. The inset shows the total spin accumulation and the dashed lines indicate the thermal equilibrium spin accumulation  $c$ .

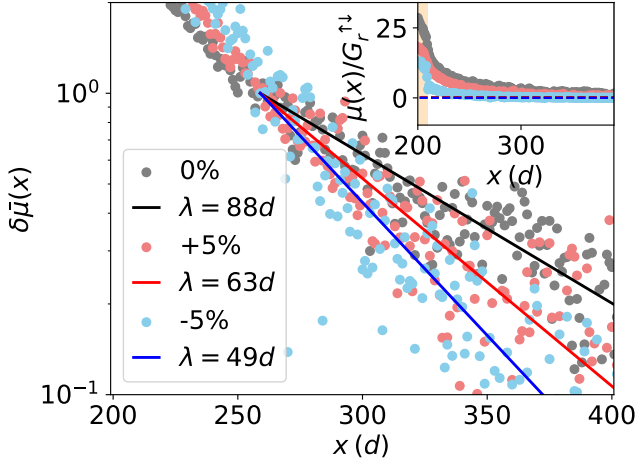


FIG. 5. Spatial dependence of the electrical SHT-induced nonequilibrium spin accumulation for three magnetic states under different strain conditions. In the main plot, the y-axis is on a logarithmic scale. The extracted spin diffusion length  $\lambda$ , found with Eq. (8), of each case is represented in the legend. The inset depicts the spatial dependence of the nonequilibrium spin accumulation on the nonlogarithmic axis.

for the SHT mechanism. As we discussed earlier, in SHT experiments, the odd component of the spin voltage,  $\delta\bar{\mu} = \delta\bar{\mu}(x, +\mathbf{p}) - \delta\bar{\mu}(x, -\mathbf{p})$ , is measured, and thus the background thermal spin signal does not appear in the spin accumulation data.

Figure 5, shows the spatial dependence of the spin accumulation for three magnetic states. We find that in

the SHT mechanism, we also get a finite spin signal in the biaxial EP AFM case. As we mentioned before, in the biaxial EP AFM case, each magnon branch is linearly polarized, which means that no spin angular momentum can be carried by them. However, in a biaxial EP AFM system, the SHT mechanism may still generate a finite spin signal through a coherent beating oscillation between two orthogonal linearly polarized magnon eigenmodes [57, 60, 90]. A finite spin signal can be observed if two magnon modes, with similar frequency but different wave vectors, on the two acoustic-like magnon branches, with linear polarization, pair up and combine to an effective elliptical polarized magnon mode. Therefore, the spin torque in this case must be strong enough to excite a pair of magnons at two acoustic-like magnon branches around the  $\Gamma$  point. This situation is different in the other two FM cases, where it is enough to only overcome the magnon band gap of the lower acoustic-like magnon branch.

Such finite magnon spin transport in EP AFM systems has recently been observed in the EP phase of hematite thin films [57, 90]. Similar experiments in 2D EP AFM cases will shed light on the exotic magnon transport within such a system.

We extract the magnon diffusion length in three magnetic states for SHT mechanism with fitting the spin accumulation with Eq. (8), see Table III.

TABLE III. The magnon spin diffusion length normalized to the lattice constant,  $\lambda/d$ , of three magnetic states for SSE and SHT mechanisms

Mechanism/Strain	0%	+5%	-5%
Thermal SSE	$68.3 \pm 0.1$	$57.4 \pm 0.1$	-
Electrical SHT	$88 \pm 3$	$63 \pm 3$	$49 \pm 3$

Note that all transport simulations have been conducted at the same background temperature  $T_0 = 1$  K, while the critical temperatures, or equivalently the magnon band gap at the  $\Gamma$  point, of the three magnetic states are different; see Eq. (7). This means that the effective temperature of magnons, or number of thermal magnons, in these three cases are different. The effect of this can be seen in Fig. 4, where there is a larger background spin signal, as shown by the dashed lines in the inset, in the unstrained EP FM state (gray) compared to the +5% strain with OOP FM state (red).

In general, high-frequency magnons have shorter lifetimes compared to low-energy ones [53, 91, 92]. Our analysis shows that the magnon spin diffusion length, listed in Table III, is shorter in the SSE mechanism compared to the SHT mechanism. This can be explained by the fact that in the thermal SSE mechanism, mostly incoherent magnons with a wide range of frequencies and momenta are generated, whereas in the electrical SHT mechanism, mainly low-frequency coherent magnon modes with a longer lifetime are generated.

For magnons excited by the SHT mechanism, the life-



time is the largest in the unstrained case which has a lower magnon band gap and thus lower frequencies compared to magnons of the strained cases with higher magnon band gaps, see Fig. 3.

Although the quantitative magnon spin diffusion length  $\lambda$  found in this article is tied to our chosen material parameter set, we expect that the qualitative behavior holds for a large range of vdW magnetic materials.

## V. SUMMARY AND CONCLUDING REMARKS

In this article, we have studied the effect of strain on a  $\text{CrCl}_3$  bilayer using atomistic spin dynamics simulations. First, we computed magnon dispersions and critical temperatures of the three magnetic states of the bilayer system. Second, we computed spin signals generated by thermal SSE and electrical SHT mechanisms in these three magnetic states. From the results we conclude that the unstrained bilayer shows the longest propagation length and the lowest critical temperature.

We show the high tunability of magnon dispersion re-

lations, magnetic state, critical temperature, and spin signal using mechanical strains in bilayer vdW magnetic systems. Based on our research for  $\text{CrCl}_3$  bilayer, we propose that the strain-dependent magnetic states in layered vdW magnetic systems can be monitored by spin transport measurements.

These magnetic layers also serve as an intriguing platform for studying magnon propagation in the presence of nonuniform mechanical strains that may create the coexistence of different magnetic states in the same system. These characteristics demonstrate the significant potential of vdW magnetic layers for the next generation of magnon-based nanotechnology.

## ACKNOWLEDGMENTS

V. B. acknowledges R. F. L. Evans and A. Meo for helpful discussions. This work has been supported by the Norwegian Financial Mechanism 2014 - 2021 under the Polish - Norwegian Research Project NCN GRIEG “2Dtronics” no. 2019/34/H/ST3/00515.

## APPENDIX: COMPUTING CRITICAL TEMPERATURE

The magnetic ground state for each strain case is obtained using a classical Monte Carlo algorithm with a zero-field cooling procedure [44]. To determine the critical temperature,  $T_c$ , we use specific heat calculations implemented in the VAMPIRE code. In Fig. A1, we present the temperature-dependent specific heat for three magnetic states. The critical temperature for each case is determined by the divergence in the corresponding specific heat. The value of the critical temperature in 2D magnetic systems is mainly governed by the magnetic anisotropies and NN Heisenberg exchange interactions. These parameters are smallest in the unstrained case and largest at  $-5\%$  strain, as also reflected in their critical temperatures.

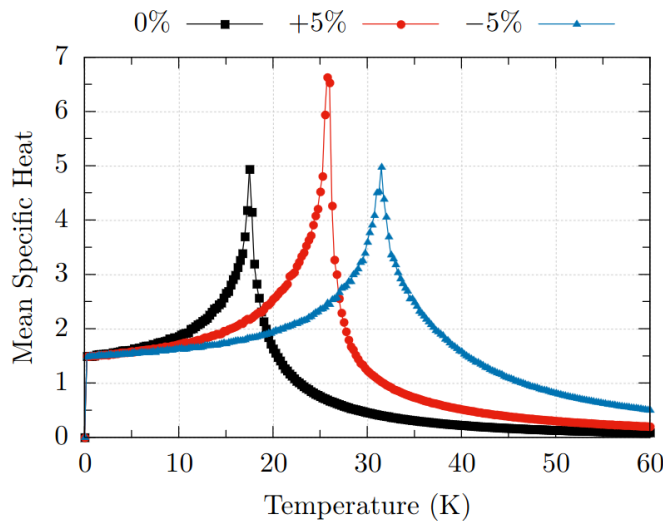


FIG. A1. The mean specific heat for the three magnetic states, see Table I. We estimate the critical temperatures as  $T_c^{0\%} \approx 17.8$  K for the EP FM state,  $T_c^{+5\%} \approx 26.0$  K for the OOP FM state, and  $T_c^{-5\%} \approx 31.8$  K for the EP AFM state.

- 
- [1] A. Avsar, H. Ochoa, F. Guinea, B. Özyilmaz, B. J. van Wees, and I. J. Vera-Marun, Colloquium: Spintronics in graphene and other two-dimensional materials, *Rev. Mod. Phys.* **92**, 021003 (2020).
- [2] N. Mounet, M. Gibertini, P. Schwaller, D. Campi, A. Merkys, A. Marrazzo, T. Sohier, I. E. Castelli, A. Ceperlotti, G. Pizzi, and N. Marzari, Two-dimensional materials from high-throughput computational exfoliation of experimentally known compounds, *Nat. Nanotechnol.* **13**, 246–252 (2018).
- [3] M. Gibertini, M. Koperski, A. F. Morpurgo, and K. S. Novoselov, Magnetic 2D materials and heterostructures, *Nat. Nanotechnol.* **14**, 408–419 (2019).
- [4] C. Gong and X. Zhang, Two-dimensional magnetic crystals and emergent heterostructure devices, *Science* **363**, eaav4450 (2019).
- [5] A. V. Chumak, V. I. Vasyuchka, A. A. Serga, and B. Hillebrands, Magnon spintronics, *Nat. Phys.* **11**, 453 (2015).
- [6] L. J. Cornelissen, J. Liu, R. A. Duine, J. B. Youssef, and B. J. van Wees, Long-distance transport of magnon spin information in a magnetic insulator at room temperature, *Nat. Phys.* **11**, 1022 (2015).
- [7] L. J. Cornelissen, K. J. H. Peters, G. E. W. Bauer, R. A. Duine, and B. J. van Wees, Magnon spin transport driven by the magnon chemical potential in a magnetic insulator, *Phys. Rev. B* **94**, 014412 (2016).
- [8] A. A. Kaverzin, T. S. Ghiasi, A. H. Dismukes, X. Roy, and B. J. van Wees, Spin injection by spin–charge coupling in proximity induced magnetic graphene, *2D Mater.* **9**, 045003 (2022).
- [9] Y. P. Feng, L. Shen, M. Yang, A. Wang, M. Zeng, Q. Wu, S. Chintalapati, and C.-R. Chang, Prospects of spintronics based on 2D materials, *Wiley Interdiscip. Rev. Comput. Mol. Sci.* **7**, e1313 (2017).
- [10] Q. H. Wang, A. Bedoya-Pinto, M. Blei, A. H. Dismukes, A. Hamo, S. Jenkins, M. Koperski, Y. Liu, Q.-C. Sun, E. J. Telford, H. H. Kim, M. Augustin, U. Vool, J.-X. Yin, L. H. Li, A. Falin, C. R. Dean, F. Casanova, R. F. L. Evans, M. Chshiev, A. Mishchenko, C. Petrovic, R. He, L. Zhao, A. W. Tsen, B. D. Gerardot, M. Brotons-Gisbert, Z. Guguchia, X. Roy, S. Tongay, Z. Wang, M. Z. Hasan, J. Wrachtrup, A. Yacoby, A. Fert, S. Parkin, K. S. Novoselov, P. Dai, L. Balicas, and E. J. G. Santos, The Magnetic Genome of Two-Dimensional van der Waals Materials, *ACS Nano* **16**, 6960 (2022).
- [11] A. Bedoya-Pinto, J.-R. Ji, A. K. Pandeya, P. Gargiani, M. Valvidares, P. Sessi, J. M. Taylor, F. Radu, K. Chang, and S. S. P. Parkin, Intrinsic 2D-XY ferromagnetism in a van der Waals monolayer, *Science* **374**, 616–620 (2021).
- [12] A. Rodin, M. Trushin, A. Carvalho, and A. H. Castro Neto, Collective excitations in 2D materials, *Nat. Rev. Phys.* **2**, 524–537 (2020).
- [13] T. Song, Q.-C. Sun, E. Anderson, C. Wang, J. Qian, T. Taniguchi, K. Watanabe, M. A. McGuire, R. Stöhr, D. Xiao, T. Cao, J. Wrachtrup, and X. Xu, Direct visualization of magnetic domains and moiré magnetism in twisted 2D magnets, *Science* **374**, 1140–1144 (2021).
- [14] A. Gao, Y.-F. Liu, C. Hu, J.-X. Qiu, C. Tzschaschel, B. Ghosh, S.-C. Ho, D. Bérubé, R. Chen, H. Sun, Z. Zhang, X.-Y. Zhang, Y.-X. Wang, N. Wang, Z. Huang, C. Felser, A. Agarwal, T. Ding, H.-J. Tien, A. Akey, J. Gardener, B. Singh, K. Watanabe, T. Taniguchi, K. S. Burch, D. C. Bell, B. B. Zhou, W. Gao, H.-Z. Lu, A. Bansil, H. Lin, T.-R. Chang, L. Fu, Q. Ma, N. Ni, and S.-Y. Xu, Layer Hall effect in a 2D topological axion antiferromagnet, *Nature* **595**, 521–525 (2021).
- [15] M. F. Jakobsen, A. Brataas, and A. Qaiumzadeh, Electrically Controlled Crossed Andreev Reflection in Two-Dimensional Antiferromagnets, *Phys. Rev. Lett.* **127**, 017701 (2021).
- [16] M. Dupont, Y. O. Kvashnin, M. Shiranzadei, J. Fransson, N. Laflorencie, and A. Kantian, Monolayer  $\text{CrCl}_3$  as an Ideal Test Bed for the Universality Classes of 2D Magnetism, *Phys. Rev. Lett.* **127**, 037204 (2021).
- [17] J. N. Kløgetvedt and A. Qaiumzadeh, Tunable topological magnon-polaron states and intrinsic anomalous Hall phenomena in two-dimensional ferromagnetic insulators (2023).
- [18] K. S. Burch, D. Mandrus, and J.-G. Park, Magnetism in two-dimensional van der Waals materials, *Nature* **563**, 47 (2018).
- [19] X. Wang, K. Du, Y. Y. F. Liu, P. Hu, J. Zhang, Q. Zhang, M. H. S. Owen, X. Lu, C. K. Gan, P. Sengupta, C. Kloc, and Q. Xiong, Raman spectroscopy of atomically thin two-dimensional magnetic iron phosphorus trisulfide ( $\text{FePS}_3$ ) crystals, *2D Mater.* **3**, 031009 (2016).
- [20] B. Huang, G. Clark, E. Navarro-Moratalla, D. R. Klein, R. Cheng, K. L. Seyler, D. Zhong, E. Schmidgall, M. A. McGuire, D. H. Cobden, W. Yao, D. Xiao, P. Jarillo-Herrero, and X. Xu, Layer-dependent ferromagnetism in a van der Waals crystal down to the monolayer limit, *Nature* **546**, 270–273 (2017).
- [21] L. Chen, J.-H. Chung, B. Gao, T. Chen, M. B. Stone, A. I. Kolesnikov, Q. Huang, and P. Dai, Topological Spin Excitations in Honeycomb Ferromagnet  $\text{CrI}_3$ , *Phys. Rev. X* **8**, 041028 (2018).
- [22] L. Chen, J.-H. Chung, T. Chen, C. Duan, A. Schneidewind, I. Radelytskyi, D. J. Voneshen, R. A. Ewings, M. B. Stone, A. I. Kolesnikov, B. Winn, S. Chi, R. A. Mole, D. H. Yu, B. Gao, and P. Dai, Magnetic anisotropy in ferromagnetic  $\text{CrI}_3$ , *Phys. Rev. B* **101**, 134418 (2020).
- [23] L. Chen, J.-H. Chung, M. B. Stone, A. I. Kolesnikov, B. Winn, V. O. Garlea, D. L. Abernathy, B. Gao, M. Augustin, E. J. G. Santos, and P. Dai, Magnetic Field Effect on Topological Spin Excitations in  $\text{CrI}_3$ , *Phys. Rev. X* **11**, 031047 (2021).
- [24] V. Brehm, P. Sobieszczyk, J. N. Kløgetvedt, R. F. L. Evans, E. J. G. Santos, and A. Qaiumzadeh, Topological magnon gap engineering in van der Waals  $\text{CrI}_3$  ferromagnets, *Phys. Rev. B* **109**, 174425 (2024).
- [25] L. Chen, M. B. Stone, A. I. Kolesnikov, B. Winn, W. Shon, P. Dai, and J.-H. Chung, Massless Dirac magnons in the two dimensional van der Waals honeycomb magnet  $\text{CrCl}_3$ , *2D Mater.* **9**, 015006 (2021).
- [26] J. A. Schneeloch, Y. Tao, Y. Cheng, L. Daemen, G. Xu, Q. Zhang, and D. Louca, Gapless Dirac magnons in  $\text{CrCl}_3$ , *npj Quantum Mater.* **7**, 66 (2022).
- [27] G. Menichetti, M. Calandra, and M. Polini, Electrical tuning of the magnetic properties of 2D magnets: the case of  $\text{Cr}_2\text{Ge}_2\text{Te}_6$  [Phys. Rev. B (to be published)] (2023), arXiv:2312.02887 [cond-mat.str-el].



- [28] A. Edström, D. Amoroso, S. Picozzi, P. Barone, and M. Stengel, Curved Magnetism in  $\text{CrI}_3$ , *Phys. Rev. Lett.* **128**, 177202 (2022).
- [29] K. Basak, M. Ghosh, S. Chowdhury, and D. Jana, Theoretical studies on electronic, magnetic and optical properties of two dimensional transition metal trihalides, *J. Phys. Cond. Mat.* **35**, 233001 (2023).
- [30] H. Ren and G. Xiang, Strain Engineering of Intrinsic Ferromagnetism in 2D van der Waals Materials, *Nanomaterials* **13**, 2378 (2023).
- [31] L.-C. Zhang, F. Zhu, D. Go, F. R. Lux, F. J. dos Santos, S. Lounis, Y. Su, S. Blügel, and Y. Mokrousov, Interplay of Dzyaloshinskii-Moriya and Kitaev interactions for magnonic properties of Heisenberg-Kitaev honeycomb ferromagnets, *Phys. Rev. B* **103**, 134414 (2021).
- [32] B. Ma and G. A. Fiete, Antiferromagnetic insulators with tunable magnon-polaron Chern numbers induced by in-plane optical phonons, *Phys. Rev. B* **105**, L100402 (2022).
- [33] P. Shen and S. K. Kim, Magnetic field control of topological magnon-polaron bands in two-dimensional ferromagnets, *Phys. Rev. B* **101**, 125111 (2020).
- [34] G. Go and S. K. Kim, Tunable large spin Nernst effect in a two-dimensional magnetic bilayer, *Phys. Rev. B* **106**, 125103 (2022).
- [35] G. Go, S. K. Kim, and K.-J. Lee, Topological Magnon-Phonon Hybrid Excitations in Two-Dimensional Ferromagnets with Tunable Chern Numbers, *Phys. Rev. Lett.* **123**, 237207 (2019).
- [36] M. Soenen and M. V. Milošević, Tunable magnon topology in monolayer  $\text{CrI}_3$  under external stimuli, *Phys. Rev. Mater.* **7**, 084402 (2023).
- [37] S. I. Vishkayi, Z. Torbatian, A. Qaiumzadeh, and R. Asgari, Strain and electric-field control of spin-spin interactions in monolayer  $\text{CrI}_3$ , *Phys. Rev. Mater.* **4**, 094004 (2020).
- [38] A. Ebrahimian, A. Dyrdał, and A. Qaiumzadeh, Control of magnetic states and spin interactions in bilayer  $\text{CrCl}_3$  with strain and electric fields: An ab initio study, *Sci. Rep.* **13**, 5336 (2023).
- [39] F. Feringa, J. M. Vink, and B. J. van Wees, Spin Nernst magnetoresistance for magnetization study of  $\text{FePS}_3$ , *Phys. Rev. B* **107**, 094428 (2023).
- [40] F. Feringa, J. M. Vink, and B. J. van Wees, Spin-flop transition in the quasi-two-dimensional antiferromagnet  $\text{MnPS}_3$  detected via thermally generated magnon transport, *Phys. Rev. B* **106**, 224409 (2022).
- [41] T. Liu, J. Peiro, D. K. de Wal, J. C. Leutenantsmeyer, M. H. D. Guimarães, and B. J. van Wees, Spin caloritronics in a  $\text{CrBr}_3$ -based magnetic van der Waals heterostructure, *Phys. Rev. B* **101**, 205407 (2020).
- [42] W. Xing, L. Qiu, X. Wang, Y. Yao, Y. Ma, R. Cai, S. Jia, X. C. Xie, and W. Han, Magnon Transport in Quasi-Two-Dimensional van der Waals Antiferromagnets, *Phys. Rev. X* **9**, 011026 (2019).
- [43] D. K. de Wal, A. Iwens, T. Liu, P. Tang, G. E. W. Bauer, and B. J. van Wees, Long-distance magnon transport in the van der Waals antiferromagnet  $\text{CrPS}_4$ , *Phys. Rev. B* **107**, L180403 (2023).
- [44] R. F. L. Evans, W. J. Fan, P. Chureemart, T. A. Ostler, M. O. A. Ellis, and R. W. Chantrell, Atomistic spin model simulations of magnetic nanomaterials, *J. Phys. Condens. Matter* **26**, 103202 (2014).
- [45] K. Uchida, J. Xiao, H. Adachi, J. Ohe, S. Takahashi, J. Ieda, T. Ota, Y. Kajiwara, H. Umezawa, H. Kawai, G. E. W. Bauer, S. Maekawa, and E. Saitoh, Spin Seebeck insulator, *Nat. Mater.* **9**, 894–897 (2010).
- [46] E.-J. Guo, J. Cramer, A. Kehlberger, C. A. Ferguson, D. A. MacLaren, G. Jakob, and M. Kläui, Influence of Thickness and Interface on the Low-Temperature Enhancement of the Spin Seebeck Effect in YIG Films, *Phys. Rev. X* **6**, 031012 (2016).
- [47] S. M. Rezende, R. L. Rodríguez-Suárez, and A. Azevedo, Theory of the spin Seebeck effect in antiferromagnets, *Phys. Rev. B* **93**, 014425 (2016).
- [48] K. Uchida, S. Takahashi, K. Harii, J. Ieda, W. Koshibae, K. Ando, S. Maekawa, and E. Saitoh, Observation of the spin Seebeck effect, *Nature* **455**, 778 (2008).
- [49] H. Adachi, K. Uchida, E. Saitoh, and S. Maekawa, Theory of the spin Seebeck effect, *Rep. Prog. Phys.* **76**, 036501 (2013).
- [50] L. Chotorlishvili, Z. Toklikishvili, V. K. Dugaev, J. Barnaś, S. Trimper, and J. Berakdar, Fokker-Planck approach to the theory of the magnon-driven spin Seebeck effect, *Phys. Rev. B* **88**, 144429 (2013).
- [51] S. R. Etesami, L. Chotorlishvili, and J. Berakdar, Spectral characteristics of time resolved magnonic spin Seebeck effect, *Appl. Phys. Lett.* **107**, 132402 (2015).
- [52] J. Cramer, U. Ritzmann, B.-W. Dong, S. Jaiswal, Z. Qiu, E. Saitoh, U. Nowak, and M. Kläui, Spin transport across antiferromagnets induced by the spin Seebeck effect, *J. Phys. D: Appl. Phys.* **51**, 144004 (2018).
- [53] U. Ritzmann, D. Hinzke, and U. Nowak, Propagation of thermally induced magnonic spin currents, *Phys. Rev. B* **89**, 024409 (2014).
- [54] A. Mook, R. R. Neumann, J. Henk, and I. Mertig, Spin Seebeck and spin Nernst effects of magnons in non-collinear antiferromagnetic insulators, *Phys. Rev. B* **100**, 100401 (2019).
- [55] M. Weißenhofer and U. Nowak, Topology dependence of skyrmion Seebeck and skyrmion Nernst effect, *Sci. Rep.* **12**, 6801 (2022).
- [56] R. Lebrun, A. Ross, S. A. Bender, A. Qaiumzadeh, L. Baldrati, J. Cramer, A. Brataas, R. A. Duine, and M. Kläui, Tunable long-distance spin transport in a crystalline antiferromagnetic iron oxide, *Nature* **51**, 222–225 (2018).
- [57] R. Lebrun, A. Ross, O. Gomonay, V. Baltz, U. Ebels, A.-L. Barra, A. Qaiumzadeh, A. Brataas, J. Sinova, and M. Kläui, Long-distance spin-transport across the Morin phase transition up to room temperature in ultra-low damping single crystals of the antiferromagnet  $\alpha\text{-Fe}_2\text{O}_3$ , *Nat. Commun.* **11**, 6332 (2020).
- [58] J. E. Hirsch, Spin Hall Effect, *Phys. Rev. Lett.* **83**, 1834 (1999).
- [59] S. Zhang, Spin Hall Effect in the Presence of Spin Diffusion, *Phys. Rev. Lett.* **85**, 393 (2000).
- [60] V. Brehm, O. Gomonay, S. Lepadatu, M. Kläui, J. Sinova, A. Brataas, and A. Qaiumzadeh, Micromagnetic study of spin transport in easy-plane antiferromagnetic insulators, *Phys. Rev. B* **107**, 184404 (2023).
- [61] K. S. Das, J. Liu, B. J. van Wees, and I. J. Vera-Marun, Efficient Injection and Detection of Out-of-Plane Spins via the Anomalous Spin Hall Effect in Permalloy Nanowires, *Nano Lett.* **18**, 5633 (2018).
- [62] J. Sinova, S. O. Valenzuela, J. Wunderlich, C. H. Back, and T. Jungwirth, Spin Hall effects, *Rev. Mod. Phys.* **87**,

- 1213 (2015).
- [63] X. Cai, T. Song, N. P. Wilson, G. Clark, M. He, X. Zhang, T. Taniguchi, K. Watanabe, W. Yao, D. Xiao, M. A. McGuire, D. H. Cobden, and X. Xu, Atomically Thin  $\text{CrCl}_3$ : An In-Plane Layered Antiferromagnetic Insulator, *Nano Lett.* **19**, 3993 (2019).
  - [64] D. L. Esteras and J. J. Baldoví, Strain engineering of magnetic exchange and topological magnons in chromium trihalides from first-principles, *Mater. Today Electron.* **6**, 100072 (2023).
  - [65] L. Webster and J.-A. Yan, Strain-tunable magnetic anisotropy in monolayer  $\text{CrCl}_3$ ,  $\text{CrBr}_3$ , and  $\text{CrI}_3$ , *Phys. Rev. B* **98**, 144411 (2018).
  - [66] B. Hussain and M. G. Cottam, Dipole-exchange spin waves in two-dimensional van der Waals ferromagnetic films and stripes, *J. Phys. Condens. Matter* **34**, 445801 (2022).
  - [67] F. J. Buijnsters, L. J. A. van Tilburg, A. Fasolino, and M. I. Katsnelson, Two-dimensional dispersion of magnetostatic volume spin waves, *J. Phys. Condens. Matter* **30**, 255803 (2018).
  - [68] VAMPIRE software package v5 available from <https://vampire.york.ac.uk/> (2020).
  - [69] R. Cheng, J. Xiao, Q. Niu, and A. Brataas, Spin Pumping and Spin-Transfer Torques in Antiferromagnets, *Phys. Rev. Lett.* **113**, 057601 (2014).
  - [70] D. Reitz, J. Li, W. Yuan, J. Shi, and Y. Tserkovnyak, Spin Seebeck effect near the antiferromagnetic spin-flop transition, *Phys. Rev. B* **102**, 020408 (2020).
  - [71] J. Tang and R. Cheng, Absence of cross-sublattice spin pumping and spin-transfer torques in collinear antiferromagnets (2023), <https://pubs.aip.org/aip/apm/article-pdf/doi/10.1063/5.0159062/18211072/111117.1.5.0159062.pdf>.
  - [72] A. Brataas, Y. V. Nazarov, and G. E. W. Bauer, Finite-Element Theory of Transport in Ferromagnet–Normal Metal Systems, *Phys. Rev. Lett.* **84**, 2481 (2000).
  - [73] M. X. Aguilar-Pujol, S. Catalano, C. González-Orellana, W. Skowroński, J. M. Gomez-Perez, M. Ilyn, C. Rogero, M. Gobbi, L. E. Hueso, and F. Casanova, Magnon currents excited by the spin Seebeck effect in ferromagnetic EuS thin films, *Phys. Rev. B* **108**, 224420 (2023).
  - [74] A. Meo, C. E. Cronshaw, S. Jenkins, A. Lees, and R. F. L. Evans, Spin-transfer and spin-orbit torques in the Landau–Lifshitz–Gilbert equation, *J. Phys. Condens. Matter* **35**, 025801 (2022).
  - [75] V. E. Demidov, S. Urazhdin, B. Divinskiy, V. D. Bessonov, A. B. Rinkevich, V. V. Ustinov, and S. O. Demokritov, Chemical potential of quasi-equilibrium magnon gas driven by pure spin current, *Nat. Commun.* **8**, 1579 (2017).
  - [76] S. M. Rezende, A. Azevedo, and R. L. Rodríguez-Suárez, Introduction to antiferromagnetic magnons, *J. Appl. Phys.* **126**, 151101 (2019).
  - [77] V. L. Maleev, Dipole forces and critical dynamics of anisotropic ferromagnets, *Sov. Phys. JETP* **42**, 713 (1975).
  - [78] V. L. Maleev, Dipole forces in two-dimensional and layered ferromagnets, *Sov. Phys. JETP* **43**, 1240 (1976).
  - [79] Y. Yafet, J. Kwo, and E. M. Gyorgy, Dipole-dipole interactions and two-dimensional magnetism, *Phys. Rev. B* **33**, 6519 (1986).
  - [80] P. Bruno, Spin-wave theory of two-dimensional ferromagnets in the presence of dipolar interactions and magnetocrystalline anisotropy, *Phys. Rev. B* **43**, 6015 (1991).
  - [81] R. P. Erickson and D. L. Mills, Magnetic instabilities in ultrathin ferromagnets, *Phys. Rev. B* **46**, 861 (1992).
  - [82] B. A. Ivanov and E. V. Tartakovskaya, Stabilization of Long-Range Magnetic Order in 2D Easy-Plane Antiferromagnets, *Phys. Rev. Lett.* **77**, 386 (1996).
  - [83] S. Jenkins, L. Rózsa, U. Atxitia, R. F. L. Evans, K. S. Novoselov, and E. J. G. Santos, Breaking through the Mermin-Wagner limit in 2D van der Waals magnets, *Nat. Commun.* **13**, 6917 (2022).
  - [84] N. D. Mermin and H. Wagner, Absence of Ferromagnetism or Antiferromagnetism in One- or Two-Dimensional Isotropic Heisenberg Models, *Phys. Rev. Lett.* **17**, 1133 (1966).
  - [85] P. C. Hohenberg, Existence of Long-Range Order in One and Two Dimensions, *Phys. Rev.* **158**, 383 (1967).
  - [86] S. Coleman, There are no Goldstone bosons in two dimensions, *Commun. Math. Phys.* **31**, 259–264 (1973).
  - [87] L. N. Kapoor, S. Mandal, P. C. Adak, M. Patankar, S. Manni, A. Thamizhavel, and M. M. Deshmukh, Observation of Standing Spin Waves in a van der Waals Magnetic Material, *Adv. Mater.* **33**, 2005105 (2021).
  - [88] L. J. Cornelissen, J. Shan, and B. J. van Wees, Temperature dependence of the magnon spin diffusion length and magnon spin conductivity in the magnetic insulator yttrium iron garnet, *Phys. Rev. B* **94**, 180402 (2016).
  - [89] A. Brataas, H. Skarsvåg, E. G. Tveten, and E. Løhaugen Fjærbu, Heat transport between antiferromagnetic insulators and normal metals, *Phys. Rev. B* **92**, 180414 (2015).
  - [90] J. Han, P. Zhang, Z. Bi, Y. Fan, T. S. Safi, J. Xiang, J. Finley, L. Fu, R. Cheng, and L. Liu, Birefringence-like spin transport via linearly polarized antiferromagnetic magnons, *Nat. Nanotechnol.* **15**, 563 (2020).
  - [91] A. V. Chumak, *Spintronics Handbook, Second Edition: Spin Transport and Magnetism* (CRC Press, 2019) Chap. Fundamentals of magnon-based computing.
  - [92] U. Ritzmann, *Modeling spincaloric Transport: Magnon accumulation and propagation*, Ph.D. thesis, Universität Konstanz, Konstanz (2015).